

## Seismic interferometry applied to regional and teleseismic events recorded at Planchón-Peteroa Volcanic Complex, Argentina-Chile

Casas, José Augusto; Badi, Gabriela Alejandra ; Franco, Luis; Draganov, Deyan

**DOI**

[10.1016/j.jvolgeores.2020.106805](https://doi.org/10.1016/j.jvolgeores.2020.106805)

**Publication date**

2020

**Document Version**

Accepted author manuscript

**Published in**

Journal of Volcanology and Geothermal Research

**Citation (APA)**

Casas, J. A., Badi, G. A., Franco, L., & Draganov, D. (2020). Seismic interferometry applied to regional and teleseismic events recorded at Planchón-Peteroa Volcanic Complex, Argentina-Chile. *Journal of Volcanology and Geothermal Research*, 393, 1-10. Article 106805.  
<https://doi.org/10.1016/j.jvolgeores.2020.106805>

**Important note**

To cite this publication, please use the final published version (if applicable).  
Please check the document version above.

**Copyright**

Other than for strictly personal use, it is not permitted to download, forward or distribute the text or part of it, without the consent of the author(s) and/or copyright holder(s), unless the work is under an open content license such as Creative Commons.

**Takedown policy**

Please contact us and provide details if you believe this document breaches copyrights.  
We will remove access to the work immediately and investigate your claim.

# Seismic interferometry applied to regional and teleseismic events recorded at Planchón-Peteroa Volcanic Complex, Argentina-Chile

Casas, José Augusto<sup>a</sup>, Badi, Gabriela Alejandra<sup>b</sup>, Franco, Luis<sup>c</sup>, Draganov, Deyan<sup>d</sup>

<sup>a</sup>*Facultad de Ciencias Astronómicas y Geofísicas, Universidad Nacional de La Plata, CONICET, Argentina*

<sup>b</sup>*Facultad de Ciencias Astronómicas y Geofísicas, Universidad Nacional de La Plata, Argentina*

<sup>c</sup>*Observatorio Volcanológico de los Andes del Sur (OVDAS-SERNAGEOMIN), Chile*

<sup>d</sup>*Department of Geoscience and Engineering, Delft University of Technology, The Netherlands*

---

## Abstract

The Planchón-Peteroa Volcanic Complex (PPVC) is located in the Central Andes, Argentina-Chile. Even though this active volcanic system is considered one of the most dangerous volcanoes in the region, with more than twenty modest ( $VEI < 4$ ) Holocene eruptions, knowledge of its subsurface structures, internal processes, dynamics, and their relation, is still limited.

Seismic interferometry (SI) is a high-resolution technique based on analyses of the interference of the propagation seismic energy at one or many stations. SI can be used to characterize the subsurface properties of a target area. In particular, previous SI studies performed in the area of the PPVC describe specific ranges of depth; therefore, more information is required for a thorough description of the subsurface features in the area and for a better understanding of the PPVC dynamics.

---

*Email address:* [acasas@fcaglp.unlp.edu.ar](mailto:acasas@fcaglp.unlp.edu.ar) (Casas, José Augusto)

*Preprint submitted to Journal of Volcanology and Geothermal Research January 29, 2020*

We apply SI based on autocorrelations of selected regional and teleseismic events to image the subsurface structures below stations located in Argentina and Chile during 2012. The selection of the events is performed according to their location, magnitude, angle of incidence of P-wave seismic energy, and signal-to-noise ratio in the records. For each station, we extract time windows and we process them using two ranges of frequency, which are sensitive to different depth ranges.

This work describes depths and zones previously not analyzed in the area using SI methods. The results not only complement the available geological, geochemical, and geophysical information, but present new information for depths between 10 and  $\sim 750$  km depth, increasing the general knowledge of the subsurface features in the PPVC. Finally, we also propose a model for the subsurface down to the Moho, which indicates the crustal structure and the likely distribution of magma bodies in depth.

*Keywords:*

Planchón-Peteroa Volcanic Complex, Seismic Interferometry, Regional and teleseismic events, Magma storage in depth

---

## 1. Introduction

The Planchón-Peteroa Volcanic Complex -PPVC- ( $35.223^\circ$  S,  $70.568^\circ$  W; see location in [Figure 1](#)) is located in the Andes at the international border between Argentina and Chile. The PPVC is composed of three main volcanic edifices, i.e., the Azufre, the Planchón, and the Peteroa, out of which the latter is the current active volcano. The PPVC presents overlapped calderas originating from the destruction of several volcanic structures during past explosive events ([Tormey, 1989](#)). Through analyses of its historical activity and products, this volcanic system is ranked as the most hazardous volcano

113  
114  
115  
116  
117  
118  
119  
120 in Argentina ([Elissondo and Farías, 2016](#)) and the eighth most risky volcano  
121 in Chile ([Technical sheet](#), Observatorio Volcanológico de los Andes del Sur,  
122 OVDAS-SERNAGEOMIN, Chile).

123  
124 The knowledge of the PPVC has been developed by the contribution  
125 from several disciplines, i.e., geology ([Tormey, 1989](#); [Haller et al., 1994](#);  
126 [Naranjo et al., 1999](#); [Tapia Silva, 2010](#); [Haller and Risso, 2011](#)), geochem-  
127 istry ([Benavente, 2010](#); [Tassi et al., 2016](#); [Benavente et al., 2016](#)), meteorol-  
128 ogy ([Guzmán et al., 2013](#)), ash analysis ([Ramires et al., 2013](#)), seismology  
129 ([Casas et al., 2014](#); [Manassero et al., 2014](#); [Olivera Craig, 2017](#); [Casas et al.,](#)  
130 [2018, 2019](#)), gravimetry ([Tassara et al., 2006](#)), and risk analysis ([Haller and](#)  
131 [Coscarella, 2011](#)). These studies contribute to the knowledge of the eruptive  
132 history and the current subsurface conditions of this volcanic system. Nev-  
133 ertheless, the dynamics of the PPVC and their relation with the subsurface  
134 structures are still poorly understood, increasing the local risk ([Elissondo](#)  
135 [and Farías, 2016](#)).

136  
137 A description of the subsurface structures (i.e., depth, associated dimen-  
138 sions, density contrasts, etc.) is essential for developing accurate knowl-  
139 edge of the dynamics of any volcanic system. In particular, knowledge of  
140 subsurface discontinuities provides constraints for tomographic studies, for  
141 magma-ascent modeling, among others, contributing to a better inference  
142 of the subsurface conditions, and, therefore, leading to more reliable analy-  
143 ses of likely future volcanic scenarios. Based on structural-geology analyses,  
144 [Tapia Silva \(2010\)](#) describes the subsurface geological units located in the  
145 very first 10 km of the subsurface in the area of the PPVC, and presents  
146 their distribution in depth. Even though no local studies have been applied  
147 for describing the crustal structure in the PPVC, [Farías et al. \(2010\)](#) and  
148 [Giambiagi et al. \(2012\)](#) provide a crustal structure as a function of depth

and the distance from the trench in the Central Andes. They indicate the crust to be structured by four zones delimited in depth at  $\sim 12$  (upper-crust discontinuity),  $\sim 20$  (upper-lower crust discontinuity), and  $\sim 35$  (lower-crust discontinuity) km, with uncertainties smaller than 5 km. The crust-mantle discontinuity (the Moho) is estimated at  $\sim 48$  km depth, the lithosphere-asthenosphere boundary at  $\sim 75$  km depth, and the top of the subducting slab (oceanic lithosphere) at  $\sim 120$  km depth (see also [Tassara et al. \(2006\)](#)). Nevertheless, more scientific evidence is required to increase the information about the known subsurface structures, leading to a more accurate characterization of their properties, as well as to describe the subsurface features previously not analyzed. These goals motivate local studies, as the one presented in this article.

[Claerbout \(1968\)](#) has constituted a frame over which the theory of seismic interferometry developed. This passive seismic method -from here on, Seismic Interferometry by Autocorrelations (SIbyA)- suggests that the autocorrelation of a plane-wave transmission response propagating in a horizontally layered medium, recorded at the surface, allows the retrieval of the reflection response of a virtual source co-located with the recording station. SIbyA has shown to be a robust method; it has been applied to different types of seismic data, in several areas and at different scales. For example, SIbyA was applied to global- and teleseismic phases to image the subsurface at regional scales -array lengths greater than 50 km ([Ruigrok and Wapenaar, 2012](#); [Nishitsuji et al., 2016](#)), to P-wave of microseismic events to image the shallow (down to  $\sim 3$  km depth) volcanic subsurface ([Kim et al., 2017](#)), and to ambient-noise seismic data at several scales -local and regional ([Draganov et al., 2007](#); [Gorbatov et al., 2013](#); [Boullenger et al., 2014](#); [Oren and Nowack, 2017](#); [Delph et al., 2019](#)). The robustness of SIbyA has motivated its ap-

plication to local (Casas et al., 2019), regional, and teleseismic seismic data (present article) recorded in the area of the PPVC.

Nishitsuji et al. (2016) apply SIbyA to global seismic phases recorded in the eastern flank of the Peteroa volcano during 2012. They confirm the location of the Moho at  $\sim 45$ -50 km depth, and propose a deformation feature in the subducting slab in the form of detachment, shearing, necking, or any combination of them.

Casas et al. (2019) apply SIbyA to local seismic events to image the subsurface below the stations located in the Argentine and Chilean sides of the PPVC during 2012. They confirm the geological structure described for the first 4 km of the subsurface (Tapia Silva, 2010), provide information about regions of higher heterogeneity caused by faulting and complex geochemical processes, and support the presence of a magma body emplaced at  $\sim 4$  km depth (previously suggested by Benavente (2010)).

We apply SIbyA to regional and teleseismic events selected according to their location, magnitude, angles of incidence of the P-wave seismic energy at each station, and the signal-to-noise ratio in the records. The results for two different frequency ranges allow the description of the subsurface structures between  $\sim 10$  and  $\sim 750$  km depth, as well as the inference of the crustal structure and the likely location of magma bodies down to the Moho.

## 2. Data

The present application uses seismic data recorded by stations deployed in Argentina and Chile during 2012 (see station distribution in Figure 1).

The temporary deployment of seismic instruments in an area of interest is a widely used tool for reaching several goals, e.g., perform first analyses

of the propagating wavefield and the subsurface conditions, increase the number of the recording stations, extend the analyzed area, and improve the accuracy of previous results. The MalARRgue project ([Ruigrok et al., 2012](#)) was designed by institutions from The Netherlands (Delft University of Technology -TUDelft), Argentina (Comisión Nacional de Energía Atómica CNEA), and The United States (Boise State University -BSU). Its goal was imaging and monitoring the subsurface of the Malargüe region (Mendoza, Argentina), an area of high scientific interest due to peculiar volcanic and tectonic processes ([Stern, 2004](#)). The MalARRgue project consisted of a temporal deployment (from January 2012 to January 2013) of 38 stations, out of which six were deployed along the eastern flank of the PPVC (from here on, the PV array). The PV array was equipped with short-period (2 Hz) three-component (Sercel L-22) sensors.

Another source of data is provided by three broad-band stations of the Observatorio Volcanológico de los Andes del Sur (OVDAS-SERNAGEOMIN, Chile), which are located  $\sim 6$  km northwards. These stations (from here on, OVDAS array) were active during 2012, through the same period as the PV array.

### 3. Application and results

SIbyA is described by the reciprocity theorem of correlation type ([Wapenaar, 2003, 2004](#)). Based on this theorem for transient sources ([Wapenaar and Fokkema, 2006](#)), and using autocorrelation in the time domain, we obtain:

$$\begin{aligned}
& \sum_{sources} \{ [T(\mathbf{x}_A, -t) * s_i(-t) * T(\mathbf{x}_A, t) * s_i(t)] \otimes [s(-t) * s(t)]_i \} \\
& \approx -R(\mathbf{x}_A, -t) + \delta(t) - R(\mathbf{x}_A, t) \quad , \quad (1)
\end{aligned}$$

which states that the reflection response  $R(\mathbf{x}_A, t)$  can be retrieved at the station A located (at  $\mathbf{x}_A$ ) at the surface through the autocorrelation of a recorded transmitted wavefield  $T(\mathbf{x}_A, t)$ . The operator  $*$  indicates convolution,  $\otimes$  means deconvolution, and  $\delta$  is the Dirac's delta. The factor  $[s(-t) * s(t)]_i$  corresponds to the autocorrelated source time function (ASTF), which allows the deconvolution of each source time function  $s_i(t)$ .

Even though Equation 1 requires sources over the whole stationary phase area (i.e., the Fresnel Zone), seismic events present a non-uniform spatial distribution. Therefore, performing a selection of the seismic sources to be used is essential for a proper application of SIbyA. In order the transmission response of the propagating seismic energy to be accurately estimated by the vertical component of the records, we select only seismic events with P-wave seismic energy arriving (sub) vertically to a station at the surface. The retrieved reflection response (from here on,  $R_v(\mathbf{x}_A, t)$ ) is related to a seismic source co-located with the station at the surface, radiating P-wave energy (sub)vertically downwards.

A seismic source in the subsurface releases energy that propagates towards the surface, where the energy is reflected back to the subsurface. This seismic energy is reflected, refracted, converted and diffracted at the subsurface structures and heterogeneities (or the surface), part of which arrives to the recording station at the surface. Seismograms are then composed of direct waves followed by these reverberated waves. SIbyA removes the



times previous to the direct arrival, and attenuates the incoherent noise, providing reflection evidence of the location of the subsurface structures. [Figure 2a](#) depicts the application of SIbyA in an idealized horizontally layered 2-D medium, given a plane wavefield originated by a seismic source located exactly below the station. The obtained virtual reflection response can be used to estimate the depth of the reflectors located in the subsurface below the station. Based on [Nishitsuji et al. \(2016\)](#), [Figure 2b](#) shows the scenarios (except the one shown in [Figure 2a](#)) in which this methodology would (would not) retrieve seismic reflection energy: a gently dipping layer, a steep layer, a stair-like steep layer, and a steep layer with an abrupt break along its structure.

In the real Earth, neither the wave fronts are planar at local and regional scales nor is usually the subsurface horizontally layered. In highly heterogeneous zones (as, for example, the area of the PPVC; [Manassero et al. \(2014\)](#)), the location of a seismic source exactly below the station is not an imperative condition for an accurate retrieval of the subsurface reflection response  $R_v(\mathbf{x}_A, t)$  as small variations in the location of the sources do not affect the propagation of the seismic energy in the area of interest ([Fan and Snieder, 2009](#)), i.e., the vertical component of the records is still an accurate estimation of the transmission response. Therefore, sources with small P-wave angles of incidence are selected.

### 3.1. Pre-processing

Here, we obtain the input data and prepare it for the proper application of the [Equation 1](#). Using the reference seismic catalogs (IRIS and USGS), we select events that occurred during the recording period (i.e., January 2012 until January 2013) and which are characterized by a sufficiently high

160 magnitude to have a high signal-to-noise ratio in the records of each station.  
161 Due to likely variations of the local seismic wavefield in space and time, we  
162 evaluate the signal-to-noise ratio of each event at each of the stations.

163 For the selection of seismic events, we use the software JWEED (Java  
164 version of Windows Extracted from Event Data) developed by IRIS. Based  
165 on restrictions in the origin time, the location, and the magnitude, we pre-  
166 select events (see [Figure 3](#)). According to their epicentral distance, we clas-  
167 sify them in two groups. One group is composed of events with epicentral  
168 distances between  $30^\circ$  and  $120^\circ$ , and magnitudes higher than Mw. 6; each  
169 event in this group guarantees a sufficiently small P-wave ray parameter  
170 ( $< 0.08 \text{ s/km}$ ) so that seismic energy arrives (sub)vertically at a station,  
171 i.e., with incident angles  $< \sim 25^\circ$  ([Kennett et al., 1995](#)). The second group  
172 is composed of events with epicentral distances lower than  $30^\circ$  and magni-  
173 tudes higher than Mw. 5. These events present a wide range of possible  
174 P-wave angles of incidence. Therefore, we perform an examination analysis  
175 (per station) on this second group in order to select only those events with  
176 at least one P-wave phase arriving with a ray parameter smaller than the  
177 adopted threshold (i.e.,  $0.08 \text{ s/km}$ ). The ray parameters estimated by the  
178 regional velocity model ak135 ([Kennett et al., 1995](#)) are appropriate for this  
179 analysis, as the seismic energy arrives to a zone with velocities lower than  
180 those predicted by the model ([Casas et al., 2018](#)), deviating the ray paths  
181 towards the vertical. Note that once the seismic events are selected, there is  
182 no need to keep the distinction between the groups, i.e., the information pro-  
183 vided by the records are equally important (no weights are assigned during  
184 processing).

185 The origin time of the selected events is used to extract the seismic  
186 waveforms from the records of the PV and OVDAS stations. A first estimate

of the P- and S-wave arrival times for each event is calculated using the regional velocity model ak135; this estimate is then employed to manually pick accurate P- and S-wave arrival times. These times are used to compute the signal-to-noise ratio in the frequency domain ( $FSNR = A_s/A_n$ , where  $A_s$  and  $A_n$  are the signal and noise amplitude spectrums, respectively) and subsequently obtain a frequency range of a sufficiently high ratio. We request a good ( $FSNR > 4$ ) signal-to-noise ratio for the events to be processed, in order to avoid high amplitudes of events we are not interested in.

Once we obtained the origin time of the selected events and the accurate arrival times, and we examined the (sub)vertical incidence of the P-wave energy and high signal-to-noise ratio of the records, we extract the vertical-component records of the selected events at each of the used stations.

### 3.2. Processing

The vertical-component records of seismic events with P-wave energy arriving (sub)vertically at a station represent an accurate estimate of the P-wave transmission response of such propagating wavefield (provided the discontinuities are not excessively inclined; [Nishitsuji et al. \(2016\)](#)).

From the frequency range of the processing previously selected for each event at every station according to its signal-to-noise ratio in the records, we use the frequencies higher than 0.3 Hz, a threshold defined by the instrumental characteristics of the PV-array stations ([Nishitsuji et al., 2014](#)). Furthermore, we only use those frequencies which are common for all the events, i.e., [0.3 3] Hz. In order to perform a better interpretation of the results in depth, we segmented this frequency range in two sub-ranges, i.e., [0.3 0.8] Hz and [0.8 3] Hz. The separation frequency (0.8 Hz) is selected after a trial and error approach, based on the observed coherency in the

results for all the stations in advanced stages of the processing.

In order to avoid the rise of high-amplitude non-physical arrivals caused by cross-terms in the correlations, we extract the times between the first P-wave arrival (including this first arrival) and the first S-wave arrival. As an example, [Figure 4](#) shows the processing windows for the station PV04 in the frequency range  $[0.8 \text{ } 3] \text{ Hz}$ .

As the information provided by each of the events is equally important, we normalize the processing windows according to their vertical flux of seismic energy. Therefore, all the events will contribute in the summation process in [Equation 1](#).

As suggested by [Equation 1](#), we estimate and deconvolve the ASTF from each of the autocorrelated time windows. The ASTF of each event is estimated by the main lobe and its secondary monotonously decreasing amplitudes, as shown in [Figure 5](#) for the vertical component of station AD2 and the frequency range  $[0.3 \text{ } 0.8] \text{ Hz}$ . A dominance of the main lobe in the autocorrelated deconvolved traces is observed after deconvolution. These features close to  $0 \text{ s}$  are amplitudes remaining from the deconvolution relevant to the Dirac’s delta. Therefore, we remove them through windowing, i.e., muting the monotonously decreasing amplitudes relevant to the  $0 \text{ s}$  lobe. However, high amplitudes are still present at early times, i.e., down to  $\sim 10 - 15 \text{ s}$ . These arrivals might be multiples of reflections at the crustal discontinuities and the crust-mantle boundary (the Moho). We then apply predictive deconvolution in order to attenuate these multiples (as also implemented by [Nishitsuji et al. \(2016\)](#) for the same area).

SIbyA is based on the autocorrelation of time windows extracted from the records of selected seismic events. Despite an appropriate selection of the seismic event and the P-window, note that this autocorrelation trace could

contain non-physical arrivals at times equal to the time interval between two P-wave phase arrivals (as, for example, PP or PcP phases), reducing the quality of the results. However, these time intervals are a function of the epicentral distance of the events. The seismic events used in this application present a wide range of epicentral distances, so that the non-physical arrivals are located at different times in the autocorrelations, leading to a destructive interference of their energy during stacking (Kim et al., 2019; Tork Qashqai et al., 2019).

In addition, converted waves (e.g., P-to-S and S-to-P) might also contribute to the retrieved result in the autocorrelated traces. However, provided we correlate vertical-component data, non-physical arrivals from S-wave converted energy are expected to be attenuated on these zero-offset results (Delph et al., 2019). Furthermore, we choose to autocorrelate only (sub)vertical energy on the vertical components. This further limits recording S-wave arrivals; even though a transmission path from an earthquake source to the stations might contain S-waves, the final leg of the transmission path before being detected on the vertical components of the stations will contain little to no S-wave energy. When such arrivals are reflected by the Earth’s free surface, and consecutively by impedance contrasts in the subsurface, they will also be characterized by little to no conversions to S-waves. Thus, by choosing for autocorrelation only (sub)vertical arrivals at the stations, we naturally suppress the presence in the retrieved results of cross-terms due to correlation of P- and S-wave arrivals thus obtaining mainly retrieved P-waves on the vertical component and S-waves on the horizontal components of the stations. Nevertheless, in order to provide evidence of the attenuation of these cross terms, as well as for testing the stability of our seismic results, we also apply SIbyA to the P and SH wave-

fields associated to each of the seismic sources (as applied by [Kim et al. \(2019\)](#)). We employ the three component records at a station and the location of the selected seismic sources to estimate the P and SH wavefields ([Kennett, 1991](#)). Shallow P- and S-wave velocities are required for estimating these wavefields. For (sub)vertical incident seismic energy, even though shallow velocities would not be accurately known, small variations of selected velocities do not cause big changes on the results ([Kennett, 1991](#)). Then, estimates of P and SH wavefields are sufficiently accurate. Thus, we apply the same processing scheme as for the vertical component but to the estimated wavefields. For the P wavefield, we use the same processing time window as for the vertical-component data, i.e., enclosing the first P-wave arrival and its seismic coda; for the SH wavefield, we use the same window size but enclosing the first S-phase arrival and its seismic coda. Note that P- and SH-wavefield estimation requires three-component data. As we have access to the three-component records of the PV stations only, the results using these estimated wavefields might be significant for this array exclusively.

The last step in the application of [Equation 1](#) is stacking the resulting autocorrelated traces for each station, which enhances the energy from the stationary phase area. We use phase-weighted stacking ([Schimmel and Paulssen, 1997](#); [Schimmel and Gallart, 2003](#)) for a better treatment of spurious out-of-phase arrivals compared to the classical linear stacking ([Delph et al., 2019](#); [Andrés et al., 2019](#)). [Figure 6a](#) and [Figure 6b](#) show the pre-stack panel (deconvolved and windowed autocorrelated traces) and the stacked traces for PV05 and CRI stations, which use P-wavefield data in the frequency range  $[0.3, 0.8]$  Hz and vertical-component data for  $[0.8, 3]$  Hz, respectively. Provided the stations of each array are relatively close to each

other, we also stacked the individual retrieved reflection trace per array in an attempt to further increase the signal-to-noise ratio of retrieved events.. [Figure 6c](#) and [Figure 6d](#) show the results for the OVDAS array using vertical-component data in the  $[0.3 \text{ } 0.8]$  Hz frequency range and the results using the P-wavefield data for the PV array in the  $[0.8 \text{ } 3]$  Hz frequency range, respectively.

#### 4. Interpretation and discussion

Aiming to compare the seismic results with the known features of the subsurface, we transform the time axis of the results to depth through construction and utilization of a velocity model. This model is composed of velocities provided by the regional model ak135 for depths greater than 60 km, and a modified version of the model obtained by [Bohm et al. \(2002\)](#) for shallower depths (see [Figure 7](#)).

[Figure 8](#) (right) shows the results for the PV and OVDAS arrays for each processing frequency range and each employed source of data (i.e., vertical component, P wavefield, and/or SH wavefield). Provided the complex impedance contrast with depth expected for the area of the PPVC, and the possible presence of non-physical arrivals, we only seek for the dominant amplitudes on the obtained reflection responses (i.e., local maximum amplitudes on the envelope of the resulting signal), which are potentially related to the main subsurface discontinuities. Average energy is computed for overlapping running windows; a candidate local maximum is selected when the averages of several consecutive windows are more than double the seismic energy for earlier consecutive windows. From the maximums selected automatically, we select manually the accepted local maximum amplitudes.

The lowest frequency range (i.e.,  $[0.3 \text{ } 0.8]$  Hz) gives us the possibility to describe the subsurface between  $\sim 30$  and  $\sim 750$  km depth, whereas the results for the frequency range  $[0.8 \text{ } 3]$  Hz allow us to interpret the subsurface features for depths between 10 km and the Moho. The minimum depth limit is set by the smeared delta-function (central-lobe monotonously decreasing) amplitudes removed after deconvolution. The maximum depth limit is set by significant attenuation of the seismic amplitudes at later times.

The interpretation of the results for each frequency range is performed through contrast of the seismic results and the expected location of the known subsurface features based on the geodynamic scenario and the available geological information for the area of the PPVC (Ferrán and Martínez, 1962; Tassara et al., 2006; Farías et al., 2010; Benavente, 2010; Tapia Silva, 2010; Giambiagi et al., 2012; Bostock, 2013; Deuss and Woodhouse, 2004; Faccenna et al., 2017; Jackson et al., 2018).

For each array, the obtained seismic results (see Figure 8, right) for the vertical component and the P and/or SH wavefields show dominant amplitudes (i.e., local maximum amplitudes on the waveform envelopes) in common, which we classify as potential subsurface impedance contrasts.

Note that the SH-wavefield results are not shown in Figure 8a (i.e., for  $[0.3 \text{ } 0.8]$  Hz frequency range). The SH-wavefield results are not coherent over the stations of the PV array. This might be caused by higher attenuation of the S-wave energy in comparison to the P-wave energy in this volcanic zone for the vertically incident seismic energy; then, attenuation would seriously affect S-wave coherency on the autocorrelations traces. Therefore, for the lower frequency range, the interpretation of the potential subsurface features is performed using the vertical-component and P-wavefield results for the PV array and the vertical-component results for the OVDAS array.



For the shallowest depths in the results, the multiples, although attenuated after predictive deconvolution, might still be significant, likely challenging the identification of the amplitudes representing primaries. Thus, for the shallowest depths, our interpretation is based on analyses of the spatial correlation between the arrivals in the seismic results and the known subsurface discontinuities. For arrivals at the later times, two considerations limit the possibility of them being multiples. First, the target volcanic area presents high attenuation effects (Manassero et al., 2014); therefore, long paths are highly attenuated. Second, based on Zoeppritz's equations (Shuey, 1985) and provided vertical incidence of the propagating seismic energy, refracted (i.e., transmitted) energy represent  $\sim 90\%$  of such propagated energy. Thus, the seismic energy relevant to later multiples or higher-order multiples is significantly reduced. These effects led us to infer that multiples at later times are highly attenuated, making those multiples most likely unidentifiable.

For the lower frequency range, the interpretation of the shallowest (down to  $\sim 200$  km) section of the subsurface is the most intricate as a consequence of the number of discontinuities reflecting energy and the likely presence of multiples. However, the close location of the identified features in the seismic results and the known subsurface features lead us to the interpretation of the Moho discontinuity at  $\sim 50$  km depth, a low-velocity zone (LVZ) at  $\sim 100$  km depth down to the top of the subducting slab at  $\sim 120$  km depth, and the bottom of the subducting slab at  $\sim 200$  km. Even though the available information points to the lithosphere-asthenosphere boundary being at  $\sim 75$  km depth (Tassara et al., 2006; Giambiagi et al., 2012), it emerges ambiguous in our results (see the shallowest empty rectangle in Figure 8a) likely due to hydration originating by the subducting slab at these depths (Gilbert et al., 2006), or the presence of multiples from the crustal structure.

The results for this frequency range evidence the presence of the Lehmann discontinuity (Deuss and Woodhouse, 2004) at  $\sim 270$  km depth, the 410 km and 660 km discontinuities, as well as three extra discontinuities named Reflector A, Reflector B, and Reflector C in Figure 8a. Reflector A is located around 325 km depth; we think this is relevant to the discontinuity previously identified by Havens (1999) for the same area, which might be an evidence of ancient subducted oceanic crust (Williams and Revenaugh, 2005). Reflector B is located at  $\sim 480$  km depth; given its location and relatively low amplitude, it is probably a multiple from a shallower reflector. Reflector C is located at  $\sim 600$  km depth; its distinguished amplitude guides us to think it is not a multiple of any previous arrival. The bottom of the transition zone (i.e., around 660 km depth) would present its own topography as a consequence of an ancient subducting slab moving horizontally at these depths, then undergoing thickening and folding (Faccenna et al., 2017). Reflector C might be indicating the top of this feature.

The OVDAS array is located  $\sim 6$  km to the north of the PV array, composed of half the stations of the PV array. The results for OVDAS array for the two used frequency ranges are similar to those for the PV array, which evidences that main subsurface features do not change largely along the volume separating them.

Even though dipping structures in the subsurface restrict the reflection energy arriving at the surface, we clearly identify the depth of the top and bottom of the subducting slab. Therefore, two hypotheses arise. One hypothesis suggests a stair-like subduction (Figure 2b-3), according to which the top and the bottom of the oceanic slab present horizontal (or gently inclined) regions. This hypothesis, though, would not explain the lack of seismicity at the longitude of the stations and depths of analysis (*US Geo-*

logical Survey; Nishitsuji et al. (2016)). A second hypothesis proposes a slab deformation in the form of detachment, shearing, necking, or any combination (see Figure 2b-4, Nishitsuji et al. (2016)). However, more information is required to elucidate the proper interpretation.

For the second range of frequencies (i.e., [0.8 3] Hz), we also use vertical-component data for the PV and OVDAS arrays, as well as P- and SH-wavefield data for PV array. In this case, coherent similar results are obtained from all those sources of data (see Figure 8b, right). Note that, opposite to [0.3 0.8] Hz results, SH results for [0.8 3] Hz also provide interpretable information about the subsurface reflectors. Even though the higher the frequencies, the greater the expected attenuation effect (Schön, 2015), the interpreted propagation distances are shorter for this frequency range; therefore, coherent energy arises on the SH results.

The interpretation of the results for the second frequency range is based on the average depth of the identified reflectors, the available scientific information about the subsurface in the PPVC (e.g., Ferrán and Martínez (1962); Benavente (2010); González-Vidal et al. (2018)), the proposed structure of the crust for the area (Gilbert et al., 2006; Tassara et al., 2006; Farías et al., 2010; Giambiagi et al., 2012), and the physics of magma storage in the crust (Jackson et al., 2018).

The results for both arrays for this frequency range indicate six dominant amplitudes. Those located at  $\sim 13$ ,  $\sim 18$ , and  $\sim 37$  km depth agree with the depth of intra-discontinuity in the upper crust (rigid-ductile discontinuity), the intra-crustal discontinuity (between the upper and lower crust), and the intra-discontinuity in the lower crust (rigid-ductile discontinuity), respectively.

Jackson et al. (2018) models the formation, storage, and chemical differ-

entiation of magma in the Earth’s crust. According to the physics of magma storage, the melt fraction is not homogeneously distributed with depth. A high percentage of melt is located in the very upper part of a reservoir, a low percentage is located through most of the reservoir, while a solid area is present in the lowest part. The seismic results are most probably evidence of the solid lower section of the reservoir (Jackson et al., 2018). Because of this, we speculate that magma could be stored right above some of the identified reflectors (see Figure 8b), in particular the one located at  $\sim 28$  km depth, as it is not associated with any of the main discontinuities of the crust.

The seismic results also show the location of two reflectors at  $\sim 46$  and  $\sim 52$  km depth; we interpret these reflectors as the top of the MASH (Melting, Assimilation, Storage and Homogenization zone, previously imaged by Gilbert et al. (2006) for this area) and the Moho, respectively. The MASH zone is composed of low-velocity zones (Hildreth and Moorbath, 1988) which supports the negative amplitudes of the reflector identified at  $\sim 46$  km depth, as well as the presence of a blurred Moho arrival (Gilbert et al., 2006). Finally, following Cashman et al. (2017) and González-Vidal et al. (2018), we interpret those areas between zones of likely storage of magma as transfer zones via dikes.

Our results support the information obtained for the subsurface in the area (Yuan et al., 2006; Ward et al., 2013; González-Vidal et al., 2018) which indicates (although with a limited resolution) low-velocity zones for approximately the same range of depths.

The resolution of the results is a function of the uncertainties in the velocity model, as well as the quality of the data and the processing applied. We estimate the uncertainty of our interpretation based on the width of the

identified features in the seismic results. This strategy not only accounts for the vertical resolution, according to which the pulse relevant to a discontinuity might be wider in case of small differences in the arrival times at the traces to be stacked, but also for the horizontal resolution. The energy from the Fresnel zone interferes constructively to provide the resulting seismic trace. This zone is larger for deeper discontinuities. This means that a zone that we describe as vertically below a station should be understood as starting vertically below a station and extending laterally on both sides of the vertical to include the Fresnel zone. As a result, a zone that we interpret as (sub-)horizontal or locally deformed below a station, might actually be lying away from the vertical up to the extend of half the Fresnel zone at that depth. The features on the results for the lower frequency range present an average width of  $\sim 12$  km for depths below 350 km, and  $\sim 33$  km for higher depths; the features for the higher frequency range present an average width of  $\sim 2.7$  km. Provided the close spatial correlation of our results with the geological information available for the area, we infer that the (composed -vertical and horizontal) resolution of our results is sufficiently high.

Because the interpretations performed in this article are based on the available scientific information for the area of the PPVC in addition to the obtained seismic results, [Figure 8](#) represents a reasonable subsurface model for depths between 10 and 750 km. We expect this model to be used as a starting point for more accurate estimation of the locations of the subsurface features. It is also worth noting the importance of developing a high-resolution (P- and S-wave) velocity model for the area of the PPVC, which would allow an appropriate location of seismic events in depth as well as an efficient removal of multiples, enhancing the quality of the results. Therefore, more research (particularly, local seismic velocity -or attenuation-

tomography studies) is required to accurately locate and characterize the regions of magma storage.

## 5. Conclusions

Even though the Planchón-Peteroa Volcanic Complex (PPVC) is one of the most hazardous volcanic systems in the Central Andes, its internal processes, structures, dynamics, and their relation are still not satisfactorily understood.

We applied seismic interferometry by autocorrelation to regional and teleseismic earthquake arrivals recorded by nine stations deployed in the area of the PPVC (six in Argentina and three in Chile) during 2012. The events are selected according to their location, magnitude, angle of incidence of the P-wave energy, the signal-to-noise ratio on the results, and the related useful frequency range. The interferometric results represent virtual reflection measurements from virtual sources co-located with each of the array stations, where the virtual sources emit energy (sub) vertically down. With the virtual reflection measurement, we aimed to shed extra light on the subsurface below the PPVC. In order to perform an appropriate description of the subsurface structures below the stations, we used two frequency ranges ([0.3 0.8] Hz and [0.8 3] Hz) which are sensitive to different range of depths.

We used the lower frequency range ([0.3 0.8] Hz) to infer tectonic features, i.e., the Moho (at  $\sim 50$  km depth), the lithosphere-asthenosphere boundary ( $\sim 75$  km), the top of a low-velocity zone at  $\sim 100$  km depth, the top and bottom of the subducting slab ( $\sim 120$  and  $\sim 200$  km), the Lehmann discontinuity at  $\sim 270$  km, a discontinuity at  $\sim 330$  km depth, the 410 km discontinuity, and a layer between  $\sim 600$  and  $\sim 660$  km depth likely originating

from accumulated ancient subducting slab at these depths.

Based on the results for the higher frequencies (i.e., [0.8–3] Hz) and previous geological, geochemical, and geophysical information, we proposed a model which describes the structure of the crust and the subsurface regions storing magma bodies down to the Moho. We suggested three regions of magma emplacement right above  $\sim 13$  km,  $\sim 28$  km, and  $\sim 37$  km depth, respectively.

The present work provides valuable information about the subsurface conditions of an active volcanic system -the CVPP. We expect the obtained knowledge to be employed in future research aiming to better understand the dynamics of the CVPP.

## 6. Acknowledgments

The authors thank SERNAGEOMIN for providing earthquake data recorded by the OVDAS seismic network. The authors thank IRIS-PASSCAL for providing the seismic equipment deployed in Argentina, and the Argentine Ministry of Science, Technology and Production Innovation for the financial support connected to the transportation of the equipment. The authors thank Pierre Auger Observatory and the Department of Civil Defense of Malarge for the help during the data acquisition. The authors thank two anonymous reviewers for their valuable comments that helped improve the manuscript.

## References

Andrés, J., Draganov, D., Schimmel, M., Ayarza, P., Palomeras, I., Ruiz, M., Carbonell, R., 2019. Lithospheric image of the Central Iberian Zone

- (Iberian Massif) using Global-Phase Seismic Interferometry. Solid Earth Discussions doi:[10.5194/se-2019-107](https://doi.org/10.5194/se-2019-107).
- Benavente, O., 2010. Actividad Hidrotermal asociada a los Complejos Volcánicos Planchón-Peteroa y Descabezado Grande-Quizapu-Cerro Azul, 36S y 37°S, Zona Volcánica Sur, Chile. Universidad de Chile URL: <http://repositorio.uchile.cl/handle/2250/103949>.
- Benavente, O., Tassi, F., Reich, M., Aguilera, F., Capecchiacci, F., Gutiérrez, F., Vaselli, O., Rizzo, A., 2016. Chemical and isotopic features of cold and thermal fluids discharged in the Southern Volcanic Zone between 32.5S and 36S: Insights into the physical and chemical processes controlling fluid geochemistry in geothermal systems of Central Chile. Chemical Geology doi:[10.1016/j.chemgeo.2015.11.010](https://doi.org/10.1016/j.chemgeo.2015.11.010).
- Bohm, M., Lüth, S., Echtler, H., Asch, G., Bataille, K., Bruhn, C., Rietbrock, A., Wigger, P., 2002. The Southern Andes between 36 and 40S latitude: Seismicity and average seismic velocities. Tectonophysics doi:[10.1016/S0040-1951\(02\)00399-2](https://doi.org/10.1016/S0040-1951(02)00399-2).
- Bostock, M.G., 2013. The Moho in subduction zones. doi:[10.1016/j.tecto.2012.07.007](https://doi.org/10.1016/j.tecto.2012.07.007).
- Boullenger, B., Verdel, A., Paap, B., Thorbecke, J., Draganov, D., 2014. Studying CO<sub>2</sub> storage with ambient-noise seismic interferometry: A combined numerical feasibility study and field-data example for Ketzin, Germany. Geophysics 80, Q1–Q13. doi:<https://doi.org/10.1190/geo2014-0181.1>.
- Casas, J., Draganov, D., Badi, G., Manassero, M., Olivera Craig, V., Franco



- Marín, L., Gómez, M., Ruigrok, E., 2019. Seismic interferometry applied to local fracture seismicity recorded at Planchón-Peteroa Volcanic Complex, Argentina-Chile. *Journal of South American Earth Sciences* doi:[10.1016/j.jsames.2019.03.012](https://doi.org/10.1016/j.jsames.2019.03.012).
- Casas, J.A., Badi, G., Manassero, M., Gomez, P., Draganov, D., Ruzzante, J., 2014. Characterization of Seismo-volcanic Activity in Peteroa Volcano, Central Andes Argentina-Chile. *Earth Sciences Research Journal* 18, 335–336. URL: [https://www.researchgate.net/publication/299381773\\_Characterization\\_of\\_Seismo-volcanic\\_Activity\\_in\\_Peteroa\\_Volcano](https://www.researchgate.net/publication/299381773_Characterization_of_Seismo-volcanic_Activity_in_Peteroa_Volcano)
- Casas, J.A., Mikesell, T.D., Draganov, D., Lepore, S., Badi, G.A., Franco, L., Gómez, M., 2018. Shallow S-Wave Velocity Structure from Ambient Seismic Noise at Planchón-Peteroa Volcanic Complex, Argentina-Chile. *Bulletin of the Seismological Society of America* 108, 2183–2198. doi:<https://doi.org/10.1785/0120170281>.
- Cashman, K.V., Sparks, R.S.J., Blundy, J.D., 2017. Vertically extensive and unstable magmatic systems: A unified view of igneous processes. *Science* doi:[10.1126/science.aag3055](https://doi.org/10.1126/science.aag3055).
- Claerbout, J.F., 1968. Synthesis of a layered medium from its acoustic transmission response. *GEOPHYSICS* doi:[10.1016/0022-0248\(91\)90961-4](https://doi.org/10.1016/0022-0248(91)90961-4).
- Delph, J.R., Levander, A., Niu, F., 2019. Constraining crustal properties using receiver functions and the autocorrelation of earthquake-generated body waves. *Journal of Geophysical Research: Solid Earth* doi:[10.1029/2019JB017929](https://doi.org/10.1029/2019JB017929).
- Deuss, A., Woodhouse, J.H., 2004. The nature of the Lehmann discontinuity

- from its seismological Clapeyron slopes. Earth and Planetary Science Letters doi:[10.1016/j.epsl.2004.06.021](https://doi.org/10.1016/j.epsl.2004.06.021).
- Draganov, D.S., Wapenaar, K., Mulder, W., Singer, J., Verdel, A., 2007. Retrieval of reflections from seismic background-noise measurements. Geophysical Research Letters 34. doi:[10.1029/2006GL028735](https://doi.org/10.1029/2006GL028735).
- Elissondo, M., Fariás, C., 2016. Volcanic Risk assessment in Argentina, in: Cities on Volcanoes IX, Puerto Varas, Chile. URL: [https://www.citiesonvolcanoes9.com/fileadmin/user{}\\_upload/S1.4{}\\_Elissondo.pdf](https://www.citiesonvolcanoes9.com/fileadmin/user/_upload/S1.4{}_Elissondo.pdf).
- Faccenna, C., Oncken, O., Holt, A.F., Becker, T.W., 2017. Initiation of the Andean orogeny by lower mantle subduction. Earth and Planetary Science Letters doi:[10.1016/j.epsl.2017.01.041](https://doi.org/10.1016/j.epsl.2017.01.041).
- Fan, Y., Snieder, R., 2009. Required source distribution for interferometry of waves and diffusive fields. Geophysical Journal International 179, 1232–1244. doi:[10.1111/j.1365-246X.2009.04358.x](https://doi.org/10.1111/j.1365-246X.2009.04358.x).
- Fariás, M., Comte, D., Charrier, R., Martinod, J., David, C., Tassara, A., Tapia, F., Fock, A., 2010. Crustalscale structural architecture in central Chile based on seismicity and surface geology: Implications for Andean mountain building. Tectonics 29. doi:[10.1029/2009TC002480](https://doi.org/10.1029/2009TC002480).
- Ferrán, O.L.G., Martínez, M.V., 1962. Reconocimiento geológico de la Cordillera de los Andes entre los paralelos 35 y 38 sur, in: Anales de la Facultad de Ciencias Físicas y Matemáticas, p. 19.
- Giambiagi, L., Mescua, J., Bechis, F., Tassara, A., Hoke, G., 2012. Thrust belts of the southern Central Andes: Along-strike variations in shortening,

topography, crustal geometry, and denudation. Bulletin of the Geological  
Society of America doi:[10.1130/B30609.1](https://doi.org/10.1130/B30609.1).

Gilbert, H., Beck, S., Zandt, G., 2006. Lithospheric and upper mantle structure of central Chile and Argentina. Geophysical Journal International  
doi:[10.1111/j.1365-246X.2006.02867.x](https://doi.org/10.1111/j.1365-246X.2006.02867.x).

González-Vidal, D., Obermann, A., Tassara, A., Bataille, K., Lupi, M.,  
2018. Crustal model of the Southern Central Andes derived from ambient  
seismic noise Rayleigh-wave tomography. Tectonophysics doi:[10.1016/j.tecto.2018.07.004](https://doi.org/10.1016/j.tecto.2018.07.004).

Gorbatov, A., Saygin, E., Kennett, B.L., 2013. Crustal properties from  
seismic station autocorrelograms. Geophysical Journal International  
doi:[10.1093/gji/ggs064](https://doi.org/10.1093/gji/ggs064).

Guzmán, C., Hucailuk, C., Tamasi, M., Martínez Bogado, M., Torres,  
D., 2013. Anomalías Encontradas en los Parámetros Registrados en la  
Estación de Medición de la Terma del Volcán Peteroa, in: Actas de ICES  
IX, pp. 186–194. URL: <http://www.uncuyo.edu.ar/ices/e-ices-2>.

Haller, M.J., Coscarella, M., 2011. Análisis probabilístico  
del riesgo de erupción del volcán Peteroa mediante la aplicación de mezcla de distribuciones exponenciales. Nat. Hazards Earth Syst. Sci 9, 425–431. URL: [https://www.researchgate.net/profile/Miguel\\_Haller/publication/248702232\\_Analisis\\_probabilistico\\_del\\_riesgo\\_de\\_erupcion\\_del\\_volcan\\_peteroa/links/0046352ea9820434d7000000/Analisis-probabilist](https://www.researchgate.net/profile/Miguel_Haller/publication/248702232_Analisis_probabilistico_del_riesgo_de_erupcion_del_volcan_peteroa/links/0046352ea9820434d7000000/Analisis-probabilist).

Haller, M.J., Ostera, H.A., Pesce, A.H., Gardini, M., Folguera, A., 1994.

- 626 Vulcanoestratigrafía reciente y eruptividad del volcán Peteroa, in: Con-  
627 greso Geológico Chileno, pp. 319–323.
- 628 Haller, M.J., Risso, C., 2011. La erupción del volcán peteroa (3515's, 7018'o)  
629 del 4 de septiembre de 2010. Revista de la Asociacion Geologica Ar-  
630 gentina URL: [http://ppct.caicyt.gov.ar/index.php/raga/article/](http://ppct.caicyt.gov.ar/index.php/raga/article/view/489)  
631 [view/489](http://ppct.caicyt.gov.ar/index.php/raga/article/view/489).
- 632 Havens, E., 1999. Mantle discontinuities beneath South and Central Amer-  
633 ica. Ph.D. thesis. University of California.
- 634 Hildreth, W., Moorbath, S., 1988. Crustal contributions to arc magmatism  
635 in the Andes of Central Chile. Contributions to Mineralogy and Petrology  
636 doi:[10.1007/BF00372365](https://doi.org/10.1007/BF00372365).
- 637 Jackson, M.D., Blundy, J., Sparks, R.S., 2018. Chemical differentiation,  
638 cold storage and remobilization of magma in the Earth's crust. doi:[10.](https://doi.org/10.1038/s41586-018-0746-2)  
639 [1038/s41586-018-0746-2](https://doi.org/10.1038/s41586-018-0746-2).
- 640 Kennett, B.L., 1991. The Removal of Free Surface Interactions From Three-  
641 Component Seismograms. Geophysical Journal International doi:[10.](https://doi.org/10.1111/j.1365-246X.1991.tb02501.x)  
642 [1111/j.1365-246X.1991.tb02501.x](https://doi.org/10.1111/j.1365-246X.1991.tb02501.x).
- 643 Kennett, B.L.N., Engdahl, E.R., Buland, R., 1995. Constraints on seismic  
644 velocities in the Earth from traveltimes. Geophysical Journal International  
645 doi:[10.1111/j.1365-246X.1995.tb03540.x](https://doi.org/10.1111/j.1365-246X.1995.tb03540.x).
- 646 Kim, D., Brown, L.D., Árnason, K., Águstsson, K., Blanck, H., 2017.  
647 Magma reflection imaging in Krafla, Iceland, using microearthquake  
648 sources. Journal of Geophysical Research: Solid Earth doi:[10.1002/](https://doi.org/10.1002/2016JB013809)  
649 [2016JB013809](https://doi.org/10.1002/2016JB013809).

- Kim, D., Keranen, K.M., Abers, G.A., Brown, L.D., 2019. Enhanced Resolution of the Subducting Plate Interface in Central Alaska From Autocorrelation of Local Earthquake Coda. *Journal of Geophysical Research: Solid Earth* doi:[10.1029/2018JB016167](https://doi.org/10.1029/2018JB016167).
- Manassero, M., Badi, G., Casas, J.A., Gomez, M., Draganov, D., Ruzzante, J., 2014. Seismic attenuation around Peteroa Volcano, Argentina. *Earth Sciences Research Journal* 18, 341–342. URL: <https://www.researchgate.net/publication/299388368{ }Seismic{ }attenuation{ }around{ }Peteroa{ }Volcano{ }Argentina>.
- Naranjo, J.A., Haller, M.J., Ostera, H.A., Pesce, A.H., Sruoga, P., 1999. Geología y peligros del Complejo Volcánico Planchón-Peteroa, Andes del Sur (3515'S), Región del Maule, Chile-Provincia de Mendoza, Argentina. Servicio Nacional de Geología y Minería.
- Nishitsuji, Y., Ruigrok, E., Gomez, M., Draganov, D., 2014. Global-phase H/V spectral ratio for delineating the basin in the Malargue Region, Argentina. *Seismological Research Letters* 85, 1004–1011. URL: <http://resolver.tudelft.nl/uuid:e71c7bf6-6ade-46ed-b073-324d3dd7f99b>.
- Nishitsuji, Y., Ruigrok, E., Gomez, M., Wapenaar, K., Draganov, D., 2016. Reflection imaging of aseismic zones of the Nazca slab by global-phase seismic interferometry. *Interpretation* 4, SJ1–SJ16. URL: <http://library.seg.org/doi/10.1190/INT-2015-0225.1>, doi:[10.1190/INT-2015-0225.1](https://doi.org/10.1190/INT-2015-0225.1).
- Olivera Craig, V., 2017. Relocation of fracture seismicity in Planchón-Peteroa Volcanic Complex through optimization of the arrival-times iden-

- 675 tification and joint location techniques. Graduate thesis. Universidad Na-  
676 cional de La Plata .
- 677 Oren, C., Nowack, R.L., 2017. Seismic body-wave interferometry using noise  
678 autocorrelations for crustal structure. *Geophysical Journal International*  
679 doi:[10.1093/gji/ggw394](https://doi.org/10.1093/gji/ggw394).
- 680 Ramires, A., Elissonde, A., Trombottto Liaudat, D., 2013. Posibles escenarios  
681 de riesgo frente a la caída de cenizas volcánicas, en el modelo ganadero de  
682 la cuenca alta y media del Rio Grande, Malargüe, Mendoza, in: *Actas de*  
683 *IX*, pp. 304–320. URL: <http://www.uncuyo.edu.ar/ices/e-ices-2>.
- 684 Ruigrok, E., Draganov, D., Gomez, M., Ruzzante, J., Torres, D., Pumarega,  
685 I.L., Barbero, N., Ramires, A., Ganán, A.R.C., van Wijk, K., 2012.  
686 Malargüe seismic array: Design and deployment of the temporary ar-  
687 ray. *The European Physical Journal Plus* 127, 126. doi:[https://doi.](https://doi.org/10.1140/epjp/i2012-12126-7)  
688 [org/10.1140/epjp/i2012-12126-7](https://doi.org/10.1140/epjp/i2012-12126-7).
- 689 Ruigrok, E., Wapenaar, K., 2012. Global-phase seismic interferometry un-  
690 veils P-wave reflectivity below the Himalayas and Tibet. *Geophysical*  
691 *Research Letters* 39. doi:[10.1029/2012GL051672](https://doi.org/10.1029/2012GL051672).
- 692 Schimmel, M., Gallart, J., 2003. The use of instantaneous polarization at-  
693 tributes for seismic signal detection and image enhancement. *Geophysical*  
694 *Journal International* doi:[10.1046/j.1365-246X.2003.02077.x](https://doi.org/10.1046/j.1365-246X.2003.02077.x).
- 695 Schimmel, M., Paulssen, H., 1997. Noise reduction and detection of weak,  
696 coherent signals through phase-weighted stacks. *Geophysical Journal In-*  
697 *ternational* doi:[10.1111/j.1365-246X.1997.tb05664.x](https://doi.org/10.1111/j.1365-246X.1997.tb05664.x).

- 698 Schön, J.H., 2015. Physical properties of rocks: Fundamentals and principles  
699 of petrophysics. volume 65. Elsevier.
- 700 Shuey, R.T., 1985. Simplification of the Zoeppritz equations. Geophysics  
701 doi:[10.1190/1.1441936](https://doi.org/10.1190/1.1441936).
- 702 Stern, C.R., 2004. Active Andean volcanism: its geologic and tectonic set-  
703 ting. Revista geológica de Chile doi:[10.4067/S0716-02082004000200001](https://doi.org/10.4067/S0716-02082004000200001).
- 704 Tapia Silva, F.F., 2010. Análisis estructural del sector occidental de la faja  
705 plegada y corrida de Malargüe en el curso superior del río Colorado de  
706 Lontué (35°18'y 35°23's), Región del Maule, Chile. Universidad de Chile  
707 URL: <http://repositorio.uchile.cl/handle/2250/103738>.
- 708 Tassara, A., Götze, H.J., Schmidt, S., Hackney, R., 2006. Three-dimensional  
709 density model of the Nazca plate and the Andean continental margin.  
710 Journal of Geophysical Research: Solid Earth doi:[10.1021/ic201714c](https://doi.org/10.1021/ic201714c).
- 711 Tassi, F., Aguilera, F., Benavente, O., Paonita, A., Chiodini, G., Caliro,  
712 S., Agosto, M., Gutierrez, F., Capaccioni, B., Vaselli, O., Caselli, A.,  
713 Saltori, O., 2016. Geochemistry of fluid discharges from Peteroa volcano  
714 (Argentina-Chile) in 2010-2015: Insights into compositional changes re-  
715 lated to the fluid source region(s). Chemical Geology doi:[10.1016/j.](https://doi.org/10.1016/j.chemgeo.2016.04.007)  
716 [chemgeo.2016.04.007](https://doi.org/10.1016/j.chemgeo.2016.04.007).
- 717 Tork Qashqai, M., Saygin, E., Kennett, B.L., 2019. Crustal Imaging With  
718 Bayesian Inversion of Teleseismic P Wave Coda Autocorrelation. Journal  
719 of Geophysical Research: Solid Earth doi:[10.1029/2018JB017055](https://doi.org/10.1029/2018JB017055).
- 720 Tormey, D., 1989. Geologic history of the active Azufre-Planchon-Peteroa

- 721 volcanic center (3515'S, Southern Andes) with implications for the devel-  
 722 opment of compositional gaps. *Asoc. Gel. Arg. Rev* , 420–430.
- 723 Wapenaar, K., 2003. Synthesis of an inhomogeneous medium from its acous-  
 724 tic transmission response. *GEOPHYSICS* doi:[10.1190/1.1620649](https://doi.org/10.1190/1.1620649).
- 725 Wapenaar, K., 2004. Retrieving the elastodynamic Green's function of an  
 726 arbitrary inhomogeneous medium by cross correlation. *Physical Review*  
 727 *Letters* 93. doi:[10.1103/PhysRevLett.93.254301](https://doi.org/10.1103/PhysRevLett.93.254301).
- 728 Wapenaar, K., Fokkema, J., 2006. Green's function representations for seis-  
 729 mic interferometry. *GEOPHYSICS* doi:[10.1190/1.2213955](https://doi.org/10.1190/1.2213955).
- 730 Ward, K.M., Porter, R.C., Zandt, G., Beck, S.L., Wagner, L.S., Minaya, E.,  
 731 Tavera, H., 2013. Ambient noise tomography across the Central Andes.  
 732 *Geophysical Journal International* doi:[10.1093/gji/ggt166](https://doi.org/10.1093/gji/ggt166).
- 733 Williams, Q., Revenaugh, J., 2005. Ancient subduction, mantle eclogite,  
 734 and the 300 km seismic discontinuity. *Geology* doi:[10.1130/G20968.1](https://doi.org/10.1130/G20968.1).
- 735 Yuan, X., Asch, G., Bataille, K., Bock, G., Bohm, M., Echtler, H., Kind,  
 736 R., Oncken, O., Wölbern, I., 2006. Deep seismic images of the Southern  
 737 Andes. *Geological Society of America Special Papers* doi:[10.1130/2006.](https://doi.org/10.1130/2006.2407(03))  
 738 [2407\(03\)](https://doi.org/10.1130/2006.2407(03)).

## 739 7. Figures



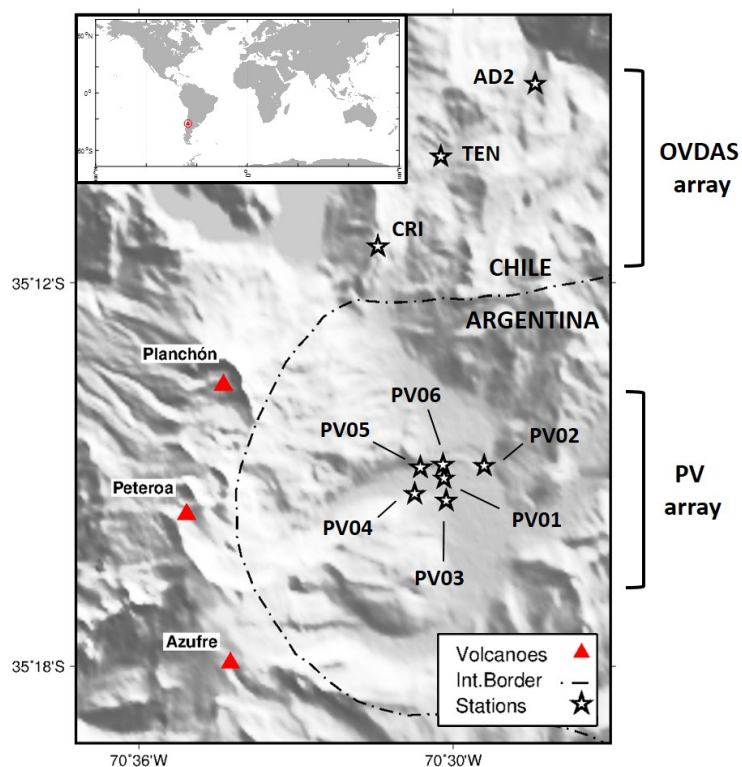


Figure 1: Distribution of the seismic stations used in the present application in relation to the main edifices of the Planchón-Peteroa Volcanic Complex (PPVC).

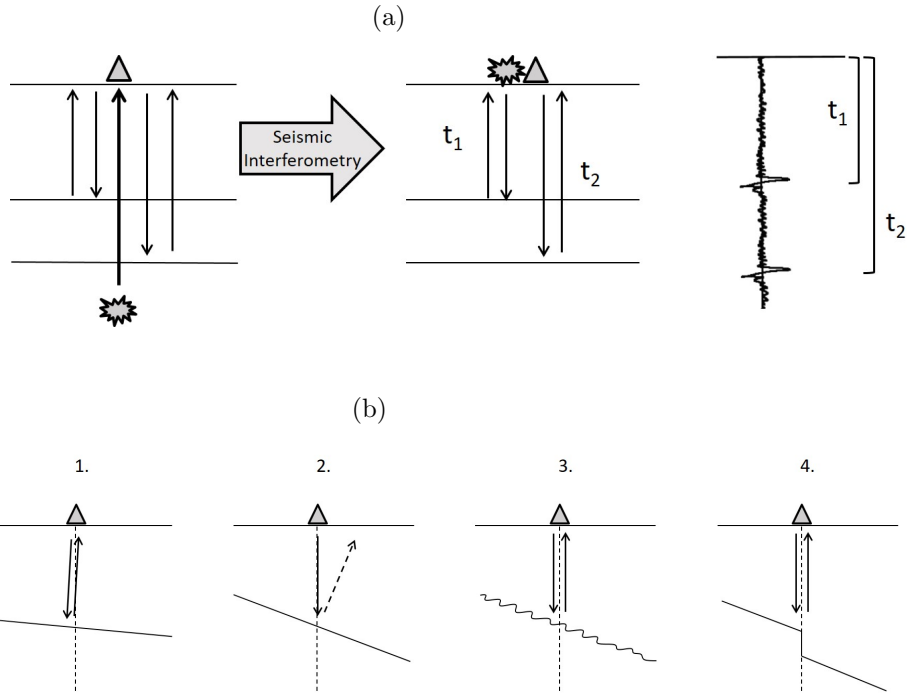


Figure 2: (a) Seismic interferometry by autocorrelation applied to vertically arriving energy in a horizontally layered medium. Parameter  $t_j$  represents the two-way travel time between the station at the surface and the reflector  $j$  in the subsurface. The autocorrelation allows the retrieval of a seismogram composed of reflected energy released by a virtual source co-located at the position of the station. Each layer is heterogeneous, which is perceived by the arriving energy at times between strong arrivals. For sake of simplicity, we show only vertical-component results with reflector multiples removed. (b) Schematic scenarios in which the applied methodology would (would not) retrieve seismic reflection energy from a subsurface layer. Solid arrows represent seismic energy leaving or arriving at the station, while a dashed arrow indicates seismic energy not arriving at the station. A dashed line shows the vertical as a reference. 1. A sub-horizontal layer; 2. A steep layer; 3. A stair-like steep layer; 4. A steep layer with an abrupt discontinuity along its structure (Nishitsuji et al., 2016).

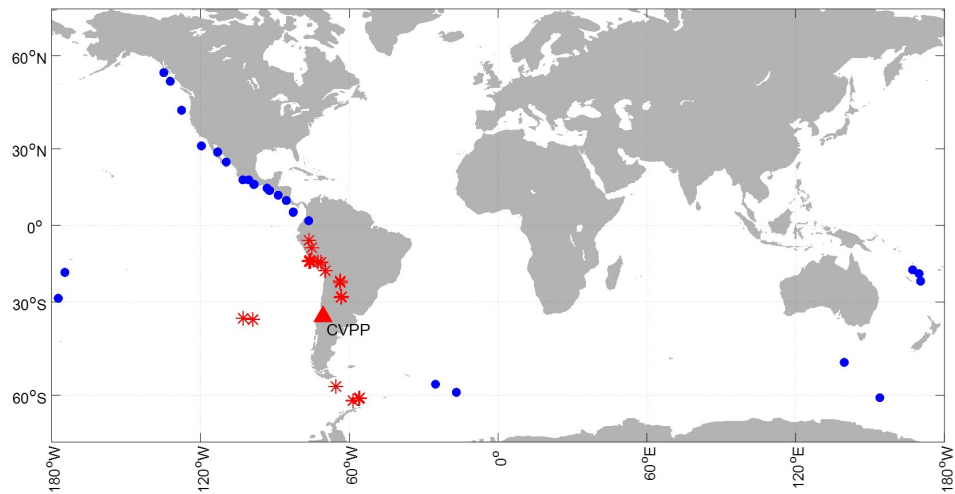


Figure 3: Location of seismic events pre-selected for the application of SIbyA in the area of the PPVC. A triangle indicates the location of the main edifices constituting the PPVC. Stars show the location of events with epicentral distances less than  $30^\circ$  and magnitudes  $M_w > 5$ . Circles indicate events with epicentral distances greater than  $30^\circ$  and less than  $120^\circ$ , and magnitudes  $M_w > 6$ .

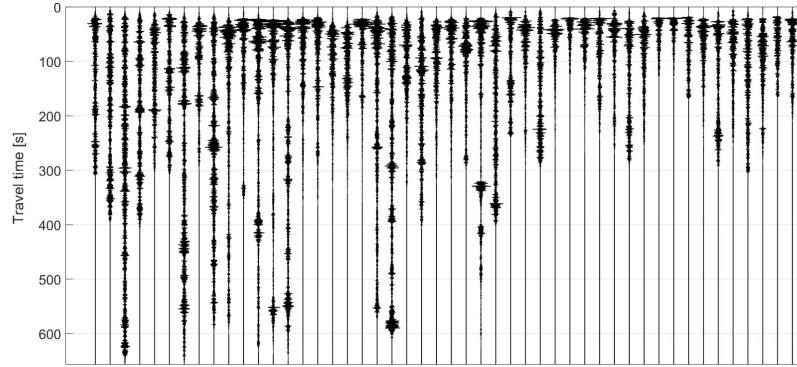


Figure 4: Processing time windows (vertical-component P-wave windows) for each of the events selected for PV04 station for frequencies  $[0.8\ 3]$  Hz. Each window is normalized according to its vertical energy flux. Vertical axis indicates propagation time. Each window is composed of a pre-event time (20 s) and the times between the first P- and S-wave arrival times.

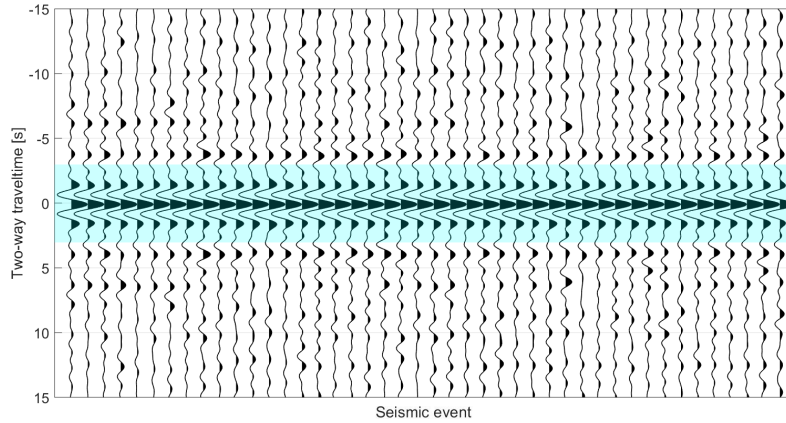
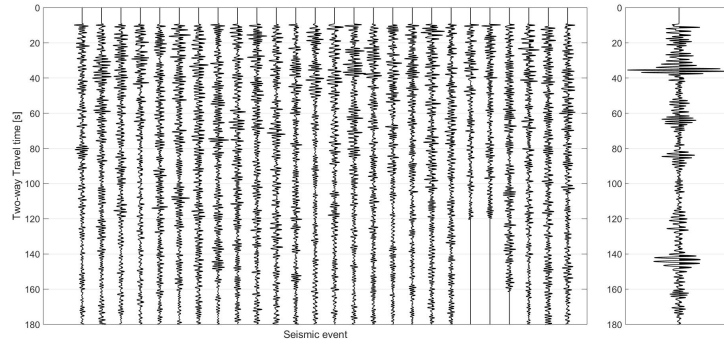
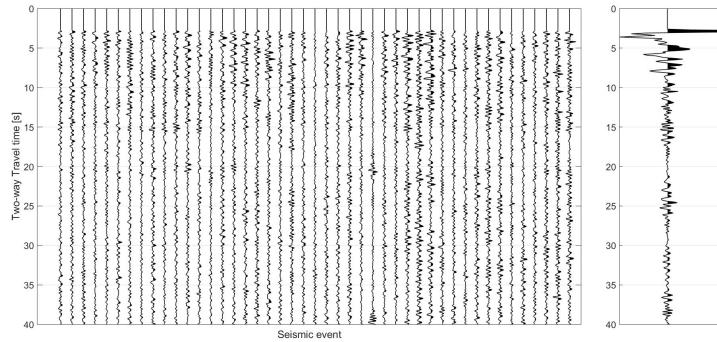


Figure 5: Autocorrelated source time functions (ASTFs) estimated for the vertical component of station AD2 for the frequency range  $[0.3\ 0.8]$  Hz. A highlighted area shows the ASTFs in the autocorrelation panel (for graphical purposes, we only show the first 15 s).

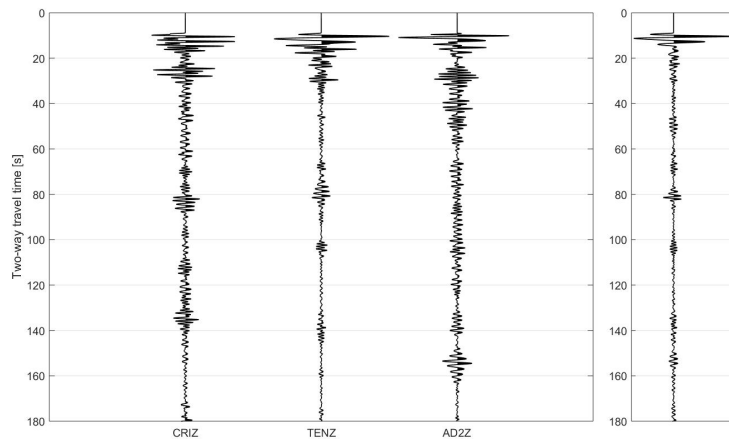
(a) PV05, P wavefield, [0.3 0.8] Hz



(b) CRI, Vertical component, [0.8 3] Hz



(c) Stack OVDAS, Vertical component, [0.3 0.8] Hz



(d) Stack PV, P wavefield, [0.8 3] Hz

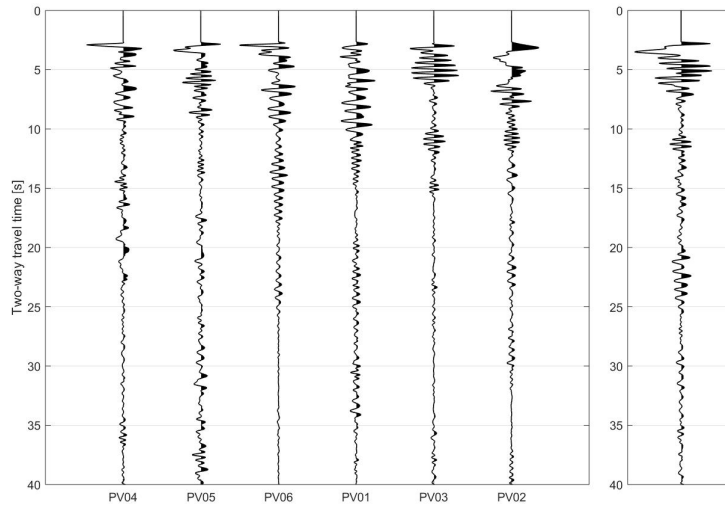


Figure 6: Pre-stacking panels (left) and stacked seismic trace (right) for (a) station PV05 using the P-wavefield data for the frequency range [0.3 0.8] Hz, and (b) station CRI using the vertical-component data for the frequency range [0.8 3] Hz. We also show the individual retrieved reflection traces at each station (left) and their stacked result (right) for (c) the OVDAS array using the vertical-component data for the frequency range [0.3 0.8] Hz, and (d) the PV array using the P-wavefield data for the frequency range [0.8 3] Hz.

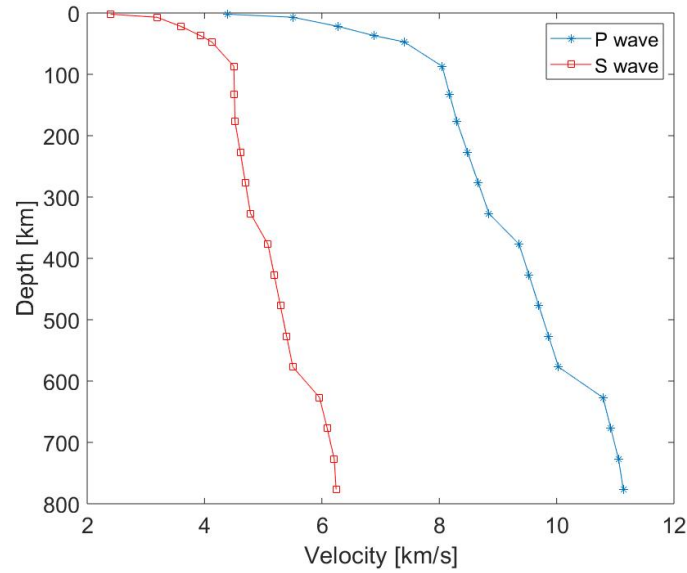


Figure 7: Velocity model used to perform the time-to-depth transformation of the retrieved zero-offset reflection traces.

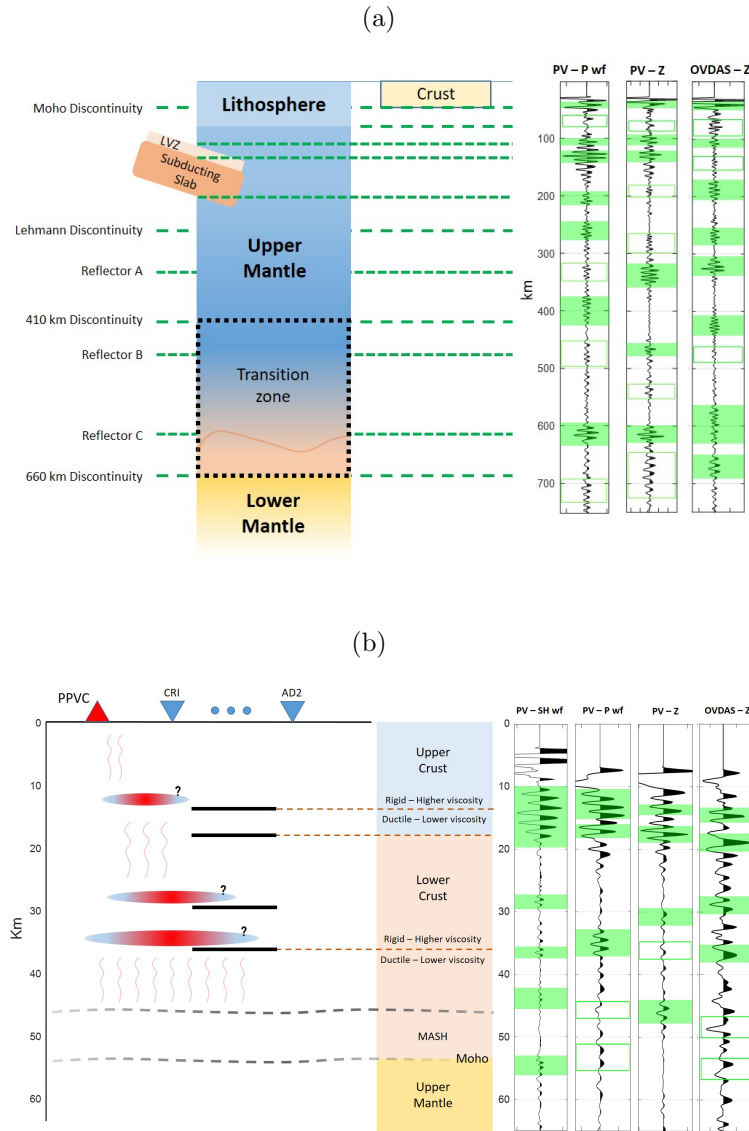


Figure 8: Interpretation of the results for [0.3 0.8] Hz, (b) [0.8 3] Hz. Filled rectangle areas in the seismic results show the local maximum amplitudes, i.e., the interpreted subsurface discontinuities below each array. Empty rectangles indicate a higher uncertainty at the identification of a discontinuity. Vertical axes are in km; the horizontal size of the interpreted features is arbitrary and it does not follow any particular scale. In (b), inverted triangles indicate the longitude of the stations, thick horizontal lines below the stations show the average depth of the reflectors interpreted in the seismic results, and dashed lines are the interpreted discontinuities between the different regions of the crust (based on [Farías et al. \(2010\)](#) and [Giambiagi et al. \(2012\)](#)). Question marks indicate zones of likely magma storage based on [Jackson et al. \(2018\)](#). MASH = Melting, Assimilation, Storage and Homogenization zone ([Gilbert et al., 2006](#)).



## Conflict of Interest and Authorship Conformation Form

Please check the following as appropriate:

- ✓ All authors have participated in (a) conception and design, or analysis and interpretation of the data; (b) drafting the article or revising it critically for important intellectual content; and (c) approval of the final version.
- ✓ This manuscript has not been submitted to, nor is under review at, another journal or other publishing venue.
- ✓ The authors have no affiliation with any organization with a direct or indirect financial interest in the subject matter discussed in the manuscript
  - The following authors have affiliations with organizations with direct or indirect financial interest in the subject matter discussed in the manuscript:

Author's name	Affiliation
CASAS, José Augusto	Facultad de Ciencias Astronómicas y Geofísicas, UNLP, CONICET, Argentina
BADI, Gabriela Alejandra	Facultad de Ciencias Astronómicas y Geofísicas, UNLP, Argentina
FRANCO, Luis	Observatorio Vulcanológico de los Andes del Sur, SERNAGEOMIN, Chile
DRAGANOV, Deyan	Department of Geoscience and Engineering, Delft University of Technology, The Netherlands

**Author statement:**

Casas, José Augusto

Conceptualization, Software, Formal analysis, Writing - Original Draft and Editing

Badi, Gabriela Alejandra

Conceptualization, Writing - Review & Editing

Franco, Luis

Resources

Draganov, Deyan

Conceptualization, Formal analysis, Writing - Review & Editing